THE JOURNAL OF BIOLOGICAL CHEMISTRY VOL. 288, NO. 39, pp. 28347–28356, September 27, 2013

Structural Basis for the Regulation of the Mitogen-activated Protein (MAP) Kinase p38α by the Dual Specificity Phosphatase 16 MAP Kinase Binding Domain in Solution*◆

Received for publication, July 3, 2013, and in revised form, August 1, 2013 Published, JBC Papers in Press, August 7, 2013, DOI 10.1074/jbc.M113.499178

Ganesan Senthil Kumar[‡], **Heiko Zettl**[‡1], **Rebecca Page**[§], **and Wolfgang Peti**[‡¶2]

From the Departments of [‡]*Molecular Pharmacology, Physiology and Biotechnology,* [§]*Molecular Biology, Cell Biology, and Biochemistry, and* [¶]*Chemistry, Brown University, Providence, Rhode Island 02912*

Background: Dual specificity phosphatases play a crucial role in MAP kinase regulation.
Results: DUSP16 (MKP7) and p38α interact in a unique manner that is different from other DUSPs.
Conclusion: DUSP16 binds p38α via an extended binding surface that includes helix α4.
Significance: This study shows that DUSPs interact differently with p38α and lays the structural basis for their differential regulation of MAPKs.

Mitogen-activated protein kinases (MAPKs) fulfill essential biological functions and are key pharmaceutical targets. Regulation of MAPKs is achieved via a plethora of regulatory proteins including activating MAPKKs and an abundance of deactivating phosphatases. Although all regulatory proteins use an identical interaction site on MAPKs, the common docking and hydrophobic pocket, they use distinct kinase interaction motif (KIM or D-motif) sequences that are present in linear, peptide-like, or well folded protein domains. It has been recently shown that a KIM-containing MAPK-specific dual specificity phosphatase DUSP10 uses a unique binding mode to interact with p38α. Here we describe the interaction of the MAPK binding domain of DUSP16 with p38α and show that despite belonging to the same dual specificity phosphatase (DUSP) family, its interaction mode differs from that of DUSP10. Indeed, the DUSP16 MAPK binding domain uses an additional helix, α-helix 4, to further engage p38α. This leads to an additional interaction surface on p38α. Together, these structural and energetic differences in p38α engagement highlight the fine-tuning necessary to achieve MAPK specificity and regulation among multiple regulatory proteins.

Ser/Thr mitogen-activated kinases (MAPKs) play central roles in a plethora of essential regulatory signaling events (1). In humans, there are 14 MAPKs, with ERK, p38, and JNK being the best studied. A major distinction for these families of MAPKs is how they are activated, with ERKs being activated by mitogens and p38s and JNKs being activated by environmental stress and inflammatory cytokines. It is their respective roles in these processes that have made MAPKs major drug targets over the last 15 years (2–6).

Dual phosphorylation of a Thr-*X*-Tyr sequence in the MAPK activation loop leads to a more than 1000-fold increase of their catalytic activity. This activation is orchestrated by a linear enzyme cascade in which MAPK kinases kinases activate MAPK kinases, which, in turn, activate the MAPKs. In contrast, the timely and spatial deactivation of MAPKs is performed by a large variety of phosphatases, including the tyrosine-specific phosphatases (kinase interaction motif-protein-tyrosine phosphatases, KIM-PTP)[3] and dual specificity phosphatases (DUSPs) (7–9). All of these activating and deactivating regulatory proteins bind MAPKs via a KIM (also known as a D-motif) (10, 11). The KIM binds to a binding site that is formed by a hydrophobic groove and an acidic patch named the common docking (CD) site; together, they are known as the KIM binding or D-motif recruitment site (12, 13). KIM sequences contain basic residues that engage the CD site and a hydrophobic motif (Φ_A-*X*-Φ_B) that engages the hydrophobic pocket. For many MAPK regulatory proteins, the KIM is an ~15-amino acid peptide sequence (*e.g.* for KIM-PTPs and MAPKKs) usually found in an unstructured N-terminal extension of the protein. The interaction of KIMs with MAPKs has been studied via multiple techniques, including x-ray crystallography as well as biomolecular NMR spectroscopy in solution (10, 13–19).

In contrast, the KIMs in DUSPs are part of well folded protein domains, the MAPK binding domains (MKBDs, ~15 kDa). DUSPs vary in size but typically contain an N-terminal MKBD and a C-terminal catalytic phosphatase domain. Of the 25 human DUSPs, 10 have a KIM-containing MKBD that mediates their direct interaction with MAPKs (8, 9). The engagement of

* This work was supported, in whole or in part, by National Institutes of Health Grant R01GM098482 (to R. P.) and R01GM100910 (to W. P.). This research was also supported by Grant RSG-08-067-01-LIB from the American Cancer Society.

◆ This article was selected as a Paper of the Week.

All chemical shifts for the MAPK binding domain of DUSP16 were deposited in the BioMagResBank under accession number 19330.

[1] Supported in part by a Feodor Lynen Research Fellowship from the Alexander von Humboldt Foundation.

[2] To whom correspondence should be addressed: Brown University, Box GE-3, Providence, RI, 02903. Tel.: 401-863-6084; Fax: 401-863-6087; E-mail: wolfgang_peti@brown.edu.

[3] The abbreviations used are: KIM, kinase interaction motif; PTP, protein-tyrosine phosphatase; DUSP, dual specificity phosphatase; CD, common docking; MKBD, MAPK binding domain; MKP, MAPK phosphatase; ITC, isothermal titration calorimetry; SAXS, small angle x-ray scattering; SEC, size exclusion chromatography; TROSY, transverse relaxation optimized spectroscopy; CSP, chemical shift perturbation.

the DUSP MKBD with a MAPK functions both to localize the DUSP catalytic phosphatase domain to the phosphorylated MAPK activation loop residues, as well as, in some cases, to enhance the activity of the DUSP catalytic domain. Multiple structures of DUSP catalytic domains have been reported (20). In contrast, far fewer MKBDs have been structurally investigated. Moreover, despite the small sample size, the three-dimensional structures of the MKBDs from DUSP6 (MKP-3) (21), DUSP10 (MKP-5) (22), and DUSP16 (MKP-7) (23) are quite different. This raises the possibility that the differences in their structures may contribute to their differential selectivity and activity toward different MAPKs. Moreover, only a single structure of a MAPK·DUSP-MKBD (*viz.* p38α·DUSP10/MKP-5 MKBD) has been determined (23). Indeed, this complex showed that although the location of MKBD binding on p38α via its structured KIM is conserved, the mode of interaction is significantly different from that observed for the linear KIM peptides of most other regulators, *e.g.* KIM-PTPs.

The limited structural similarity between the DUSP MKBDs is due, in part, to their limited sequence conservation. For example, the sequence similarity of the MKBDs from DUSP10 and DUSP16 is only 32%. These sequence differences, in addition to the differences in their structures, also suggest that their mode of binding to MAPKs may not be strictly conserved. Furthermore, as observed previously, solution state studies, in addition to crystallographic studies, often reveal new insights into the structure and function of key signaling complexes (17–19, 24). Thus, additional studies that investigate how, at a molecular level, other DUSPs interact with MAPKs are critical for elucidating the structural basis of specificity of these key regulatory proteins. Here we integrate biochemical, isothermal titration calorimetry (ITC), biomolecular NMR, and small angle x-ray scattering (SAXS) studies to determine how the MKBD of DUSP16 binds p38α in solution. Our study shows that the interaction between the MKBD of DUSP16 and p38α is stronger than those reported for KIM-PTPs peptides as well as the MKBD from DUSP10. In addition, our NMR results show that DUSP16 MKBD binding to p38α does not influence the chemical shift environment of the p38α hinge or activation loop. Furthermore, although the overall interaction modes, via helices α2 and α3 and the α2-α3 loop, are similar between the MKBDs of both DUSP16 and DUSP10, the DUSP16 MKBD interacts more extensively and includes residues in helix α4. Taken together, although this is only the second study describing the interaction of a DUSP MKBD with a MAPK, this work has identified important structural differences in how these related MKBDs bind p38α that likely reflect the subtle structural and dynamic fine-tuning needed to achieve the tight regulation of MAPK activity in the cell.

EXPERIMENTAL PROCEDURES

Protein Cloning, Expression, and Purification—The coding sequences of DUSP16 MAP MKBD (corresponding to residues 5–138) were amplified using PCR, digested with NdeI/XhoI, and subcloned into a pET30a vector (Novagen) with a non-cleavable C-terminal His_6 purification tag. *Escherichia coli* BL21 (DE3) RIL cells (Agilent) transformed with the expression vector for DUSP16 were grown at 37 °C in LB broth containing selective antibiotics. The proteins were overexpressed by the addition of 1 mM isopropylthio-β-D-galactoside when the optical density (A_{600}) reached 0.8 and the cultures were grown for an additional 18–20 h at 16 °C. Cells were harvested by centrifugation (6000 × *g*, 12 min, 4 °C) and stored at −80 °C until purification.

DUSP16 MKBD cell pellets were suspended in ice-cold lysis buffer (50 mM Tris, pH 8.0, 0.5 M NaCl, 5 mM imidazole, 0.1% Triton X-100 containing EDTA-free protease inhibitor tablet (Roche Diagnostics)), lysed by high pressure cell homogenization (Avestin C3 Emulsiflex), and centrifuged (35,000 × *g*, 40 min, 4 °C). The supernatant was loaded onto a HisTrap HP column (GE Healthcare) pre-equilibrated with 50 mM Tris, pH 8.0, 0.5 M NaCl, and 5 mM imidazole (Buffer A) and was eluted using a linear gradient of Buffer B (50 mM Tris, pH 8.0, 0.5 M NaCl, 0.5 M imidazole). Fractions containing the protein were pooled, concentrated, and further purified using size exclusion chromatography (SEC, Superdex 75 26/60; GE Healthcare) pre-equilibrated in 20 mM phosphate buffer, pH 6.9, 0.2 M NaCl, 0.5 mM tris(2-carboxyethyl)phosphine (NMR Buffer A), 50 mM HEPES buffer, pH 6.8, 0.15 M NaCl, 5 mM DTT (NMR Buffer B/SAXS buffer), or 10 mM Tris, pH 7.5, 0.15 M NaCl, 0.1 mM EDTA, 0.5 mM tris(2-carboxyethyl)phosphine (ITC buffer) to a purity of >98%. Protein yield is ~20 mg/liter LB medium.

Uniformly ^{15}N- and $^{15}N/^{13}C$-labeled proteins were produced using the same procedure except that the cells were grown in M9 minimal medium supplemented with [^{15}N]ammonium chloride (1 g/liter) and/or D-[^{13}C]glucose (4 g/liter). $^{2}H,^{15}N$-Labeled proteins were expressed in M9 medium supplemented with [^{15}N]H_4Cl (1 g/liter) in 99% D_2O, whereas $^{2}H,^{13}C,^{15}N$-labeled proteins were expressed in M9 medium supplemented with [^{15}N]H_4Cl (1 g/liter) and D-d_7-[^{13}C]glucose (4 g/liter) in 99% D_2O. Expression and purification of p38α were carried out as described earlier (14, 19, 24–27).

Complexes of $^{2}H,^{15}N$-labeled/unlabeled p38α with unlabeled/$^{2}H,^{15}N,^{13}C$-labeled DUSP16 MKBD, respectively, were generated by mixing equimolar ratios of the proteins followed by purification using SEC (Superdex 75 26/60, pre-equilibrated in NMR Buffer B). The mutant DUSP16 MKBD (H71A/S72A) was generated using QuikChange mutagenesis (Agilent Technologies) and verified by sequencing (Beckman Coulter). The DUSP16 MKBD H71A/S72A mutant was expressed and purified as described above.

NMR Spectroscopy—All NMR spectra were recorded at 298 K on either Bruker Avance 500-MHz or Bruker Avance 800-MHz spectrometers both equipped with a TCI HCN z-gradient cryoprobe. NMR samples were prepared in NMR buffer containing 10% (v/v) D_2O. Sequence-specific backbone ^{1}H, ^{15}N, and ^{13}C resonance assignment for unbound DUSP16 MKBD (in NMR Buffer A; ~0.5 mM) was obtained by analyzing two-dimensional $^{1}H,^{15}N$ heteronuclear single quantum correlation, three-dimensional HNCA, three-dimensional HN(CO)CA, three-dimensional HNCACB, three-dimensional CBCA(CO)NH, and three-dimensional (H)CC(CO)NH (τ_m = 12 ms) spectra. Two-dimensional $^{1}H,^{15}N$ TROSY and a three-dimensional HNCA-TROSY spectrum of the unlabeled-p38α/$^{2}H,^{15}N,^{13}C$-labeled DUSP16 MKBD complex (molecular mass ≥~55 kDa; NMR Buffer B; ~0.5 mM) were used for the sequence-specific

backbone assignment of the DUSP16 MKBD in complex with p38α.

^{15}N,^{1}H NOE (heteronuclear NOE) measurements were determined from a pair of interleaved spectra acquired with or without presaturation and a recycle delay of 5 s at 500-MHz ^{1}H Larmor frequency. All NMR spectra were processed and analyzed using Topspin 2.1/3.0/3.1 (Bruker, Billerica, MA) or NMRPipe (28) and Computer Aided Resonance Assignment (CARA) or Sparky (29), respectively. Backbone amide chemical shift deviations were calculated using the formula: $\Delta\delta_{av} = \sqrt{(0.5\ ((\delta_{HN,bound} - \delta_{HN,free})^2 + 0.04\ (\delta_{N,bound} - \delta_{N,free})^2))}$.

HADDOCK Calculations—HADDOCK (30, 31) was used to dock p38α and the DUSP16 MKBD using ambiguous NMR-derived restraints. p38α (Protein Data Bank (PDB) ID 1P38 (32)) and the DUSP16 MKBD (PDB ID 2VSW) were used as inputs. Active residues were defined as those that experience a chemical shift perturbation (CSP) (greater than the mean plus 1σ) or are broadened beyond detectability and have high solvent accessibility (side chain or total accessible surface area of greater than 50%) in the unbound protein structure as calculated using the program MOLMOL (33). Active p38α residues are 116, 125, 129, 130, 133, 160, 161, 162, 163, 310, 313, and 315; active DUSP16 MKBD residues are 35, 39, 47, 49, 60, 62, 63, 67, 68, and 71. Passive residues were defined as those having a CSP or broadened beyond detectability but also a low solvent accessibility. Passive p38α residues are 79, 108, 109, 110, 111, 113, 122, 124, 159, 309, and 312; passive DUSP16 MKBD residues are 34, 48, 56, 58, 59, 61, 64, 65, 69, 70, 72, and 73. CSPs were the only experimental restraint type used in the HADDOCK calculation, and default settings were used for all docking steps.

Isothermal Titration Calorimetry—ITC experiments were performed at 25 °C using a VP-ITC microcalorimeter (MicroCal Inc.). Titrant (10 μl per injection) was injected into the sample cell over a period of 20 s with a 250-s interval between titrations to allow for complete equilibration and base-line recovery. 28 injections were delivered during each experiment, and the solution in the sample cell was stirred at 307 rpm to ensure rapid mixing. To determine the thermodynamic parameters (ΔH, ΔS, ΔG) and binding constants (K), the DUSP16 MKBD was titrated into p38α, and the data were analyzed with a one-site binding model assuming a binding stoichiometry of 1:1 using Origin 7.0 software. A nonlinear least squares algorithm and the titrant and sample cell concentrations were used to fit the heat flow per injection to an equilibrium binding equation, providing values of the stoichiometry (n), change in enthalpy (ΔH), and binding constant (K). All data were repeated in duplicate.

Small Angle X-ray Scattering—The p38α·DUSP16 MKBD complex was generated as described above. Data were collected at 0.8, 2.2, and 4.5 mg/ml. All samples were prepared within 48 h of data acquisition and stored on ice at 4 °C. All samples were filtered (0.02-μM filter, Whatman) immediately prior to data collection. All data were recorded at beamline X9 at the National Synchrotron Light Source (NSLS) using a Dectris Pilatus 300k (3.40 m from the sample for SAXS) and a Photonic Science CCD (0.47 m from the sample for wide angle X-ray scattering) detector. 20 μl of sample was continuously flowed through a 1-mm diameter capillary and exposed to an x-ray beam for 60 s. Normalization for beam intensity, buffer subtraction, and merging of the data from both detectors were carried out using PRIMUS (34). A Guinier approximation, $I(q) = I(0)\exp(-q^2R_g^2/3)$, where a plot of $\ln(I(q))$ and q^2 is linear for $q < 1.3/R_g$, was performed on at least four independent scattering trials and averaged to determine the radius of gyration. The linearity of the Guinier region and the intensity at zero scattering angle, $I(0)$, were used to validate that all samples were monodisperse in solution. $I(0)/c$, where c is concentration, was consistent for all measurements for a single complex. GNOM (35) was used to determine the pair distribution function, $P(r)$, for each complex. 24 envelopes were generated for each complex using GASBOR (36) and were aligned and averaged using the DAMAVER program suite (37).

RESULTS

The MKBD of DUSP16—As expected (23), the DUSP16 MKBD (residues 5–138, 15.9 kDa; Fig. 1*A*) showed high levels of soluble overexpression in *E. coli* and behaves as a monomer in solution as verified by SEC. NMR analysis of the DUSP16 MKBD showed that the sequence-specific backbone assignment of 123 of the 132 expected backbone amide NH pairs (93.2%, 2 prolines; excluding the C-terminal His_6 tag and a 3-residue cloning artifact) can be readily achieved (Fig. 1*B*). Interestingly, no assignment was possible for residues Cys-50–Met-54, which are part of the KIM motif, as well as for Met-5, Ile-6, Ser-100, and Phe-103. The weak intensity of peaks N-terminal to Cys-50 and C-terminal to Met-54 indicate that these peaks are likely broadened beyond detectability by conformational exchange, indicating that these residues sample multiple conformations in the μs-ms time regime in the free form of the DUSP16 MKBD. Chemical shift index calculations derived from C^α and C^β chemical shifts showed that the secondary structure elements of the DUSP16 MKBD in solution are highly similar to that observed in the DUSP16 MKBD crystal structure (23). Furthermore, ^{15}N,^{1}H NOE (heteronuclear NOE) analysis showed that the DUSP16 MKBD has very limited fast time scale (ps/ns) dynamics in its unbound form (Fig. 1*C*).

Identification of the p38α Residues That Mediate DUSP16 MKBD Binding—DUSP16 selectively inactivates JNK and p38 following stress activation. The p38α·DUSP16 MKBD complex can be readily purified by SEC and co-elutes at a retention volume expected for a 1:1 complex (Fig. 2*A*). Correspondingly, ITC measurements showed that the DUSP16 MKBD interacts tightly with p38α, with a K_D of 893 ± 230 nM (Table 1, Fig. 2*B*). To identify which residues define the binding interface of the p38α·DUSP16 MKBD complex, we used NMR spectroscopy. Specifically, [^{2}H,^{15}N]p38α was incubated with unlabeled DUSP16 MKBD, the 55.2-kDa p38α·DUSP16 MKBD complex was purified by SEC, and a two-dimensional ^{1}H,^{15}N TROSY spectrum was immediately recorded (Fig. 2*C*) (24–26). Additional experiments using [^{2}H,^{15}N]p38α·DUSP16 MKBD ratios of 1:0.5 and 1:2.5 were also performed to more accurately track the CSPs on p38α.

Direct comparison of the two-dimensional ^{1}H,^{15}N TROSY spectra of free and DUSP16 MKBD-bound p38α reveals that MKBD binding results in CSPs of 20 peaks, 13 in fast exchange and 7 with line widths broadened beyond detection (Ile-116,

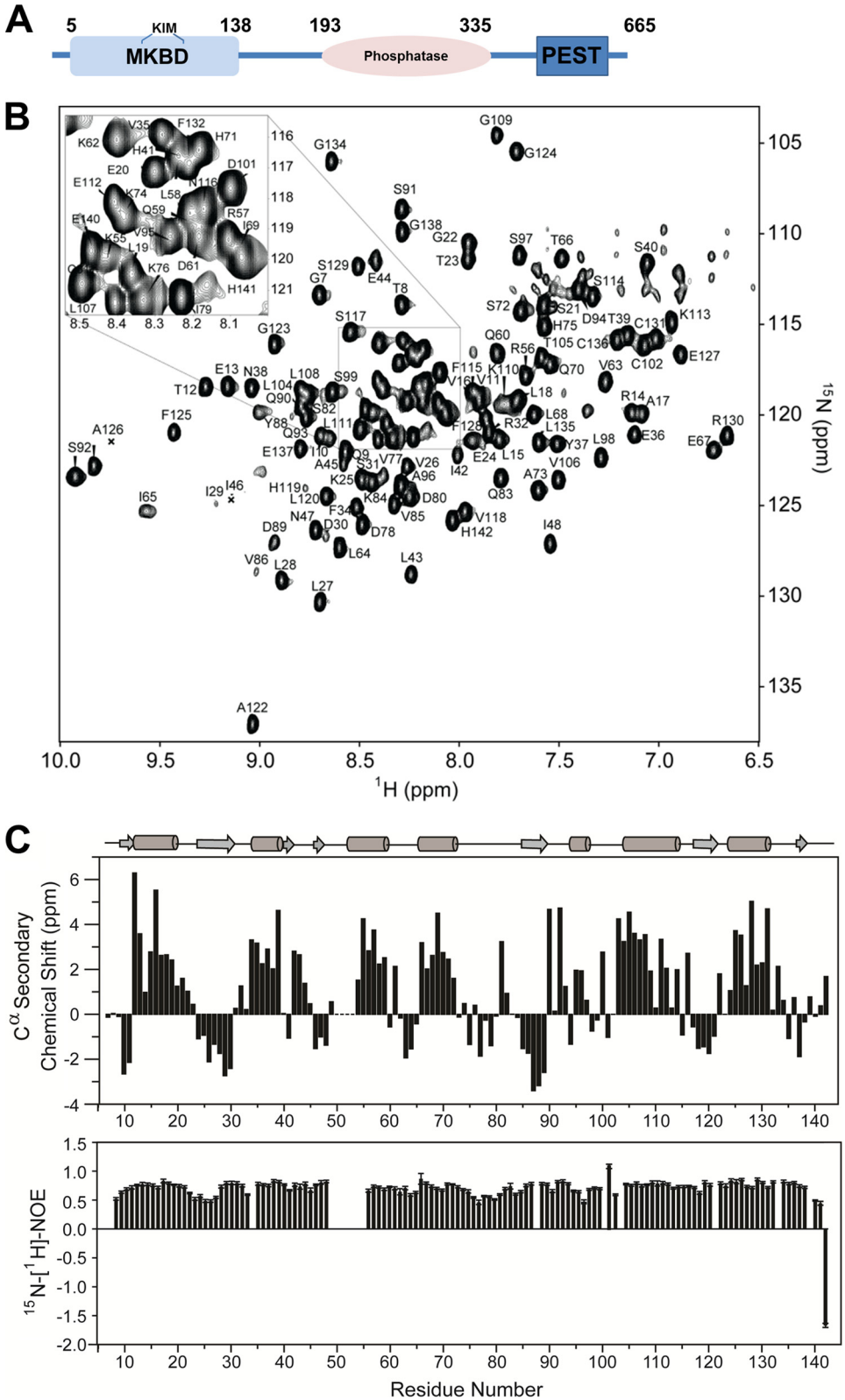

FIGURE 1. **The DUSP16 MKBD.** *A*, domain architecture of DUSP16 including the N-terminal MKBD, the catalytic phosphatase domain, and the C-terminal PEST domain. *B*, fully annotated two-dimensional ^{1}H,^{15}N heteronuclear single quantum correlation spectrum of the DUSP16 MKBD. *C*, $^{13}C_{\alpha}$ chemical shift index of the DUSP16 MKBD; secondary structural elements of the crystal structure (PDB ID 2VSW) are shown (*top panel*). ^{15}N,^{1}H NOE of the DUSP16 MKBD, showing high rigidity of the structure throughout the protein (*bottom panel*).

Lys-121, His-126, Val-127, Gln-133, Asp-161, and Ile-166; Fig. 2*D*). The perturbed residues, although largely clustered within the CD site and the hydrophobic binding groove, are decisively different from those that interact with KIM-PTPs (13–15, 18, 19). Particularly, the typical interaction with p38α residues in helix αC, strand β4, and the αC-β4 loop, residues that flank the

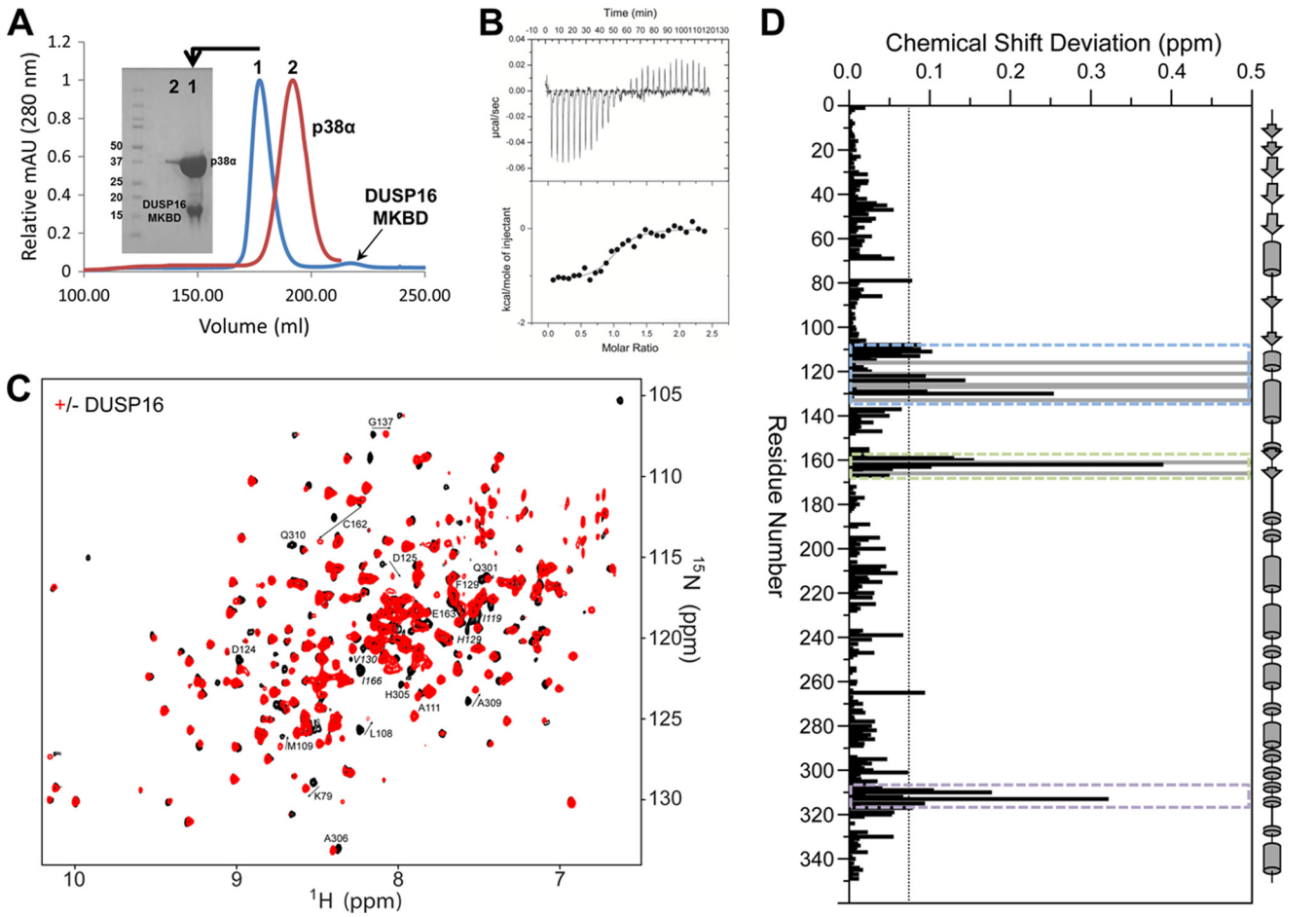

FIGURE 2. **p38α engages the DUSP16 MKBD via the KIM binding pocket, the ED site, and the CD site.** *A*, Superdex 75 26/60 SEC chromatograms are shown for p38α (*red*) and the p38α·DUSP16 MKBD complex (*blue*). The SDS-PAGE gel shows that p38α is bound to the DUSP16 MKBD in a 1:1 stoichiometric ratio and that the complex is highly pure. *mAU*, milliabsorbance units. *B*, raw isothermal titration calorimetry data (*upper panels*) and derived binding isotherm plotted *versus* the molar ratio of titrant fit using a one-site model (*lower panels*) for p38α with the DUSP16 MKBD. *C*, two-dimensional ^{1}H,^{15}N TROSY spectrum of p38α in the presence (*red*) and absence (*black*) of the DUSP16 MKBD. *D*, histogram showing the combined ^{1}H/^{15}N CSPs *versus* p38α residue upon DUSP16 MKBD binding. Residues that form the p38α KIM binding pocket (*blue dashed lines*), ED site (*green dashed lines*), and CD site (*purple dashed lines*) are highlighted. Residues with peak line widths broadened beyond detection upon titration are colored in *gray*.

TABLE 1

Thermodynamic and dissociation constants for the p38α·DUSP16 MKBD interaction derived from ITC experiments at 25 °C

Experiments were performed in duplicate.

Interaction	K_d	ΔH	$T\Delta S$	ΔG
	μM	kcal × mol^{-1}	kcal × mol^{-1}	kcal × mol^{-1}
p38α·DUSP16	0.89 ± 0.23	−1.25 ± 0.20	−7.0 ± 0.4	−8.26 ± 0.16
p38α·DUSP16$_{H71A/S72A}$	1.94 ± 0.12	3.3 ± 0.4	−11.0 ± 0.4	−7.79 ± 0.03

Φ_B binding pocket, is missing. These data show that neither the MKBD of DUSP10 (23) nor the MKBD of DUSP16 (this work) requires the Φ_B pocket for binding p38α.

Interestingly, no CSPs are detected for residues in the p38α hinge or the p38α activation loop. This shows that these regions of p38α do not experience a change in their chemical shift environment upon DUSP16 MKBD binding. This suggests that the lack of electron density for the p38α activation loop in the p38α·DUSP10 MKBD crystal structure is likely due to a change in the dynamics of the activation loop upon MKBD binding, potentially via an allosteric effect.

Identification of the DUSP16 MKBD Residues That Mediate p38α Binding—We also defined the binding interface of p38α on the DUSP16 MKBD. In this experiment, [^{2}H,^{15}N]DUSP16 MKBD was incubated with unlabeled p38α, the p38α·DUSP16 MKBD complex was purified by SEC, and a two-dimensional ^{1}H,^{15}N TROSY spectrum was recorded (Fig. 3*A*). Direct comparison of the unbound and p38α-bound DUSP16 MKBD two-dimensional ^{1}H,^{15}N TROSY spectra revealed large differences between the spectra, making chemical shift tracking analysis difficult. Thus, we completed the sequence-specific backbone assignment of the DUSP16 MKBD when bound to p38α. For these studies, [^{2}H,^{15}N,^{13}C]DUSP16 MKBD was incubated with unlabeled p38α, purified by SEC, and concentrated to ~500 μM, and a two-dimensional ^{1}H,^{15}N TROSY spectrum and a three-dimensional TROSY-HNCA spectrum were recorded. Analysis of the NMR spectra allowed for the sequence-specific backbone assignment of the p38α-bound DUSP16 MKBD and subsequent CSP analysis. As observed for unbound DUSP16 MKBD, residues Cys-50–Met-54 were also not detected when bound to p38α.

Comparison of the two-dimensional ^{1}H,^{15}N TROSY spectra of the unbound and p38α-bound DUSP16 MKBD reveals CSPs of 25 peaks, 17 in fast exchange and 8 peaks with line widths broadened beyond detection (Phe-34, Val-35, Ser-39, Ile-41, Ile-48, Asn-49, Asp-62, Ala-73; Fig. 3, *B* and *C*). The perturbed

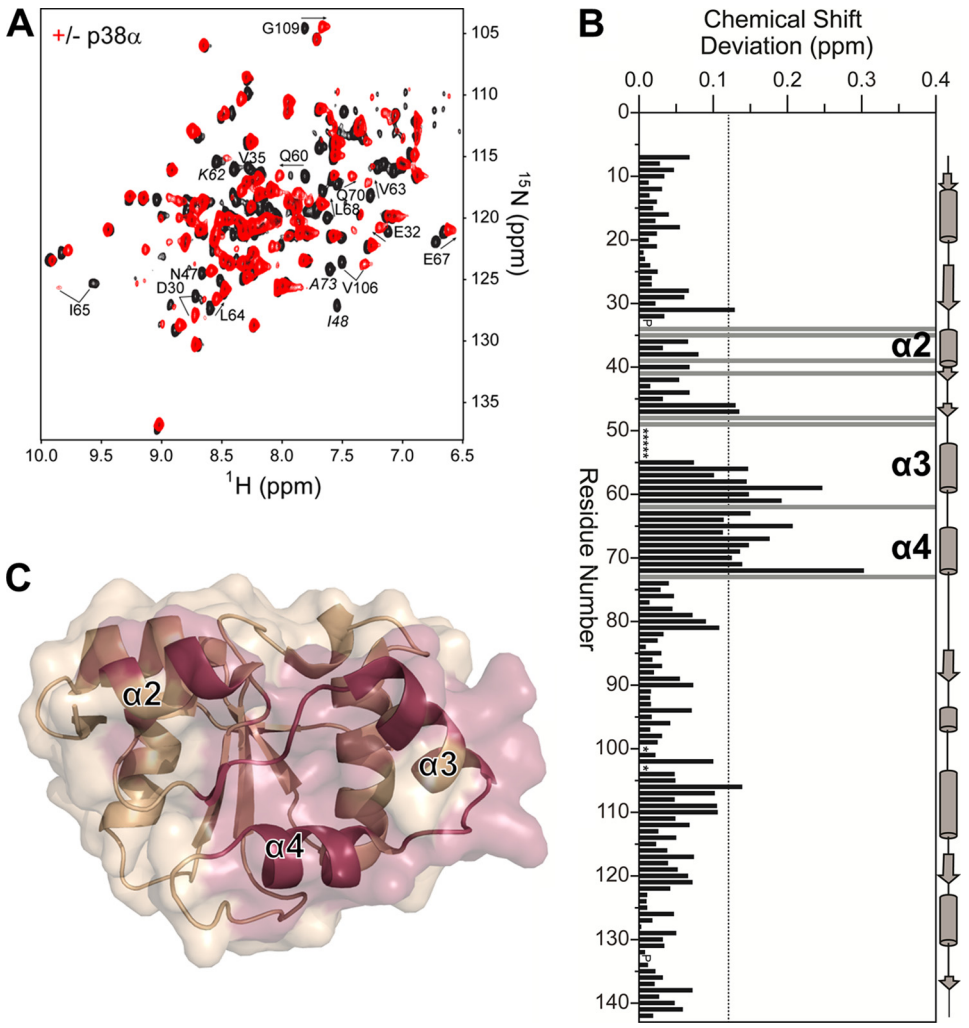

FIGURE 3. **The DUSP16 MKBD interacts with p38α via helices α2, α3, and α4.** *A*, two-dimensional ^{1}H,^{15}N TROSY spectrum of the DUSP16 MKBD in the presence (*red*) and absence (*black*) of p38α. Some residues with significant CSPs are labeled. Residues exhibiting line broadening beyond detectability are annotated in *italics*. *B*, histogram showing the combined ^{1}H/^{15}N CSPs *versus* DUSP16 MKBD residue upon p38α binding. The DUSP16 MKBD helices α2, α3, and α4 are highlighted. Residues with peak line widths broadened beyond detection upon titration are colored in *gray*. Proline residues are indicated as *P*, and unassigned residues in the unbound DUSP16 MKBD are denoted by *asterisks*. *C*, graphic surface structure of the DUSP16 MKBD (PDB ID 2VSW). Residues with CSPs or that are broadened beyond detectability are colored in *red*.

residues are clustered on helices α2, α3, and the α2-α3 loop of the DUSP16 MKBD. In addition, and different from the p38α·DUSP10 MKBD complex, residues in the DUSP16 MKBD helix α4, as well as in the α3-α4 loop that connects these helices, experience a different chemical shift environment when bound to p38α. Together, these data show that p38α binds the DUSP16 MKBD at a well defined interaction site that includes not only the previously identified interaction site (as defined by the DUSP10-MKBD·p38α complex (23)), but also includes additional residues outside this site on both p38α and DUSP16 MKBD, both of which are consistent with a strong K_D for this complex as measured by ITC (Fig. 2*B*).

The p38α·DUSP16 MKBD Complex—In the three-dimensional crystal structure of the p38α·DUSP10 MKBD complex (23), the DUSP10 MKBD adopted a conformation nearly identical as that in its unbound form, suggesting that the conformations of MKBDs change little, if at all, upon MAPK binding. Furthermore, ^{15}N,^{1}H NOE NMR data for the DUSP16 MKBD confirmed that in its unbound form, this protein is rigid. Lastly, the ^{13}Cα chemical shifts of the unbound and p38α-bound DUSP16 MKBD are essentially identical, showing that the secondary structure of the DUSP16 MKBD does not change upon p38α binding. Therefore, the DUSP16 MKBD is an ideal protein for performing NMR data-driven docking using the program HADDOCK (30, 31). We used our NMR CSP data, which identified the residues that compose the interaction interface of the p38α·DUSP16 MKBD complex, together with residue surface accessibility, to restrain the docking of the DUSP16 MKBD (PDB ID 2VSW) with p38α (PDB ID 1P38 (32)) using HADDOCK. The lowest energy cluster (HADDOCK score: −134.5 ± 6.2) contained 107 structures with a root mean square deviation of 0.5 ± 0.3 Å. The lowest energy structure from this cluster is shown in Fig. 4*A*. In this model, the DUSP16 MKBD helices α2, α3, and α4 bind to p38α in its KIM binding site. The interface between the two proteins buries 2035 Å^2 of surface area, 185 Å^2 (~10%) larger than the p38α·DUSP10 MKBD complex, which buries 1850 Å^2 of surface area and does not interact with p38α via helix α4.

To experimentally test the overall validity of the p38α·DUSP16 MKBD model, we recorded SAXS data for the p38α·DUSP16

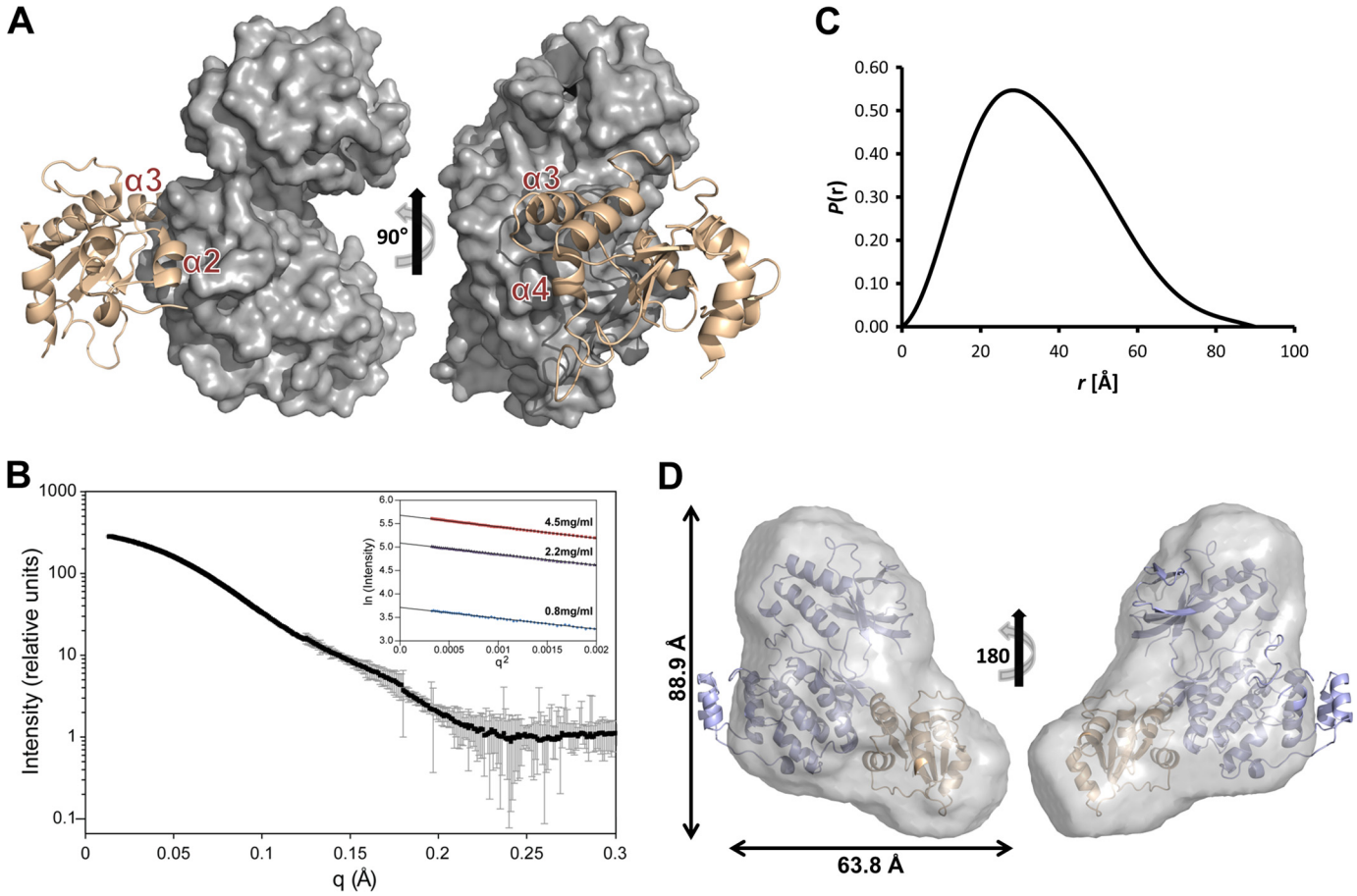

FIGURE 4. **The p38α·DUSP16 MKBD complex.** *A*, the lowest energy HADDOCK model of the p38α·DUSP16 MKBD complex. DUSP16 MKBD helices α2, α3, and α4 are highlighted. *B*, SAXS data (*I*(*q*) *versus q*) of the p38α·DUSP16 MKBD complex (*black circles*) with *error bars* (*gray lines*). *Error bars* show the experimental error based on circular averaging of the two-dimensional solution scattering data. *Inset,* Guinier plots for samples at 0.8, 2.2, and 4.5 mg/ml. *C*, *P*(*r*) function of the p38α·DUSP16 MKBD complex. *D*, *ab initio* molecular envelope (maximum dimensions are indicated) generated by GASBOR for the p38α·DUSP16 MKBD complex fitted with the lowest energy HADDOCK model of the p38α·DUSP16 MKBD complex.

TABLE 2
SAXS analysis of the p38α·DUSP16 MKBD complex

	p38α·DUSP16 MKBD
Guinier approximation	
R_g (Å)	26.7 ± 0.4
***P*(*r*) function calculation**	
Q-range (Å^{-1})	0.018–0.342
R_g (Å)	27.5
D_{max} (Å)	90
Structure modeling	
χ^2	1.01 ± 0.08
Normalized spatial discrepancy	1.05 ± 0.05

MKBD complex (Fig. 4, *B* and *C*). We compared the calculated (determined using Hydropro (38)) R_g of the lowest energy p38α·DUSP16 MKBD complex model (R_g = 28.4 Å) with the R_g determined experimentally (Table 2). The strong consistency between the R_g values is further supported by the excellent fit of the lowest energy p38α·DUSP16 MKBD HADDOCK model into the molecular envelope determined for the p38α·DUSP16 MKBD complex (Fig. 4*D*, Table 2).

Consistent with the NMR chemical shift data, the HADDOCK model of the p38α·DUSP16 MKBD complex showed that the protein-protein interface of p38α with the DUSP16 MKBD is largely similar to that of p38α with the DUSP10 MKBD (Fig. 5). Specifically, Phe-34 and Val-35 anchor the DUSP16 MKBD helix α2 to the p38α Φ_A interaction site (Fig. 5*A*). As observed in the p38α·DUSP10 MKBD complex, no interaction of the DUSP16 MKBD with the p38α Φ_B pocket is identified in solution. Furthermore, many interactions by the DUSP16 MKBD residues 47–55, which are N-terminal to and within helix α3, with p38α residues in the p38α acidic patch are clearly important for the observed nM K_D interaction between these two proteins. Finally, the p38α Φ_H interaction is conserved (Fig. 5*B*). However, and different from the p38α·DUSP10 MKBD complex, helix α4 from the DUSP16 MKBD also interacts directly with p38α (Fig. 5*C*). Indeed, even in the unbound DUSP MKBD structures (23), helix α4 of the DUSP16 MKBD is approximately one turn longer than that of the DUSP10 MKBD. Seven residues of the DUSP16 MKBD helix α4 show CSPs, and one residue (Ala-73) is broadened beyond detectability upon p38α binding. A key sequence difference between DUSP16 and DUSP10 is His-71 (Cys-218 in DUSP10). In the HADDOCK model, His-71 is predicted to make a polar interaction with p38α Gln-128 (helix α_e), which results in helix α4 being in much closer proximity to p38α. Taken together, DUSP16 MKBD helix α4 interacts with p38α residues on helices α_e and α_i. To confirm this interaction biochemically, we produced the DUSP16 MKBD H71A/S72A mutant and measured its affinity for p38α using ITC. The one-dimensional ^{1}H NMR spectra of the DUSP16 MKBD H71A/

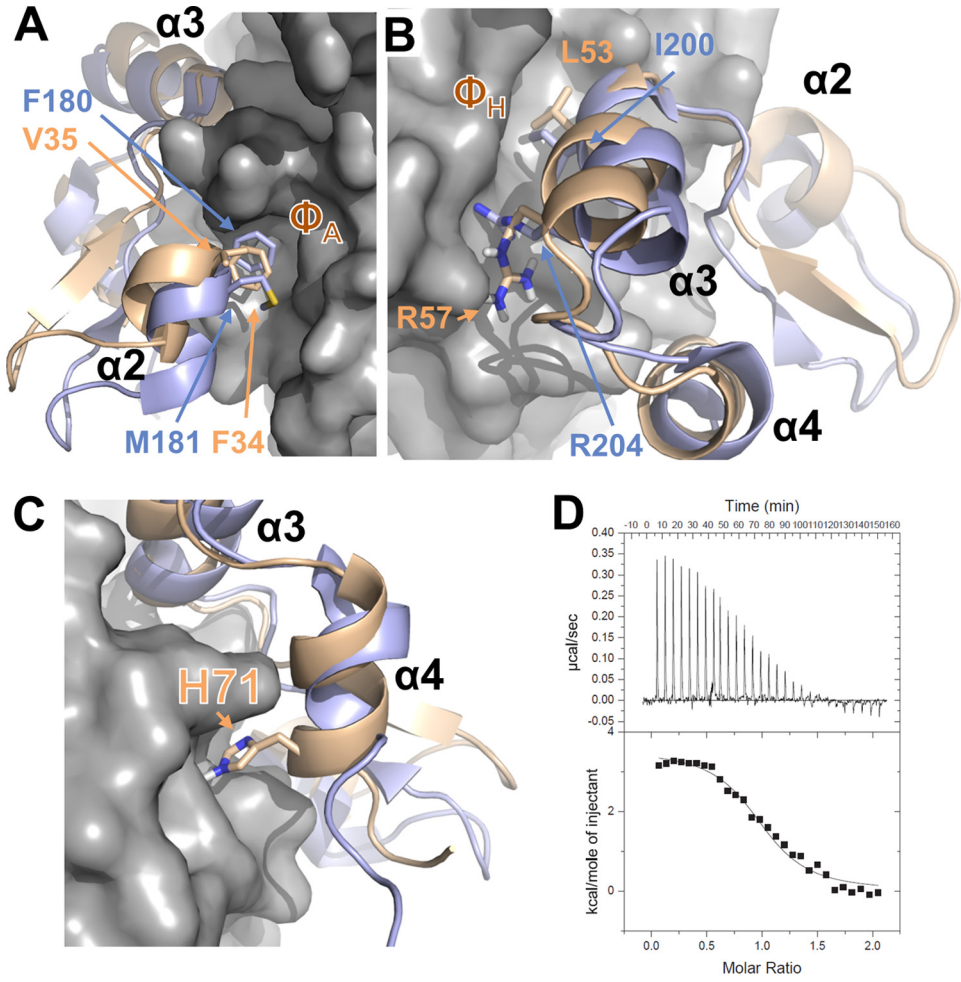

FIGURE 5. **Interaction of DUSP10 and DUSP16 with p38α is different.** *A*, overlay of the p38α·DUSP16 MKBD complex (p38α is shown as *gray surface*; DUSP16 MKBD is shown as a *wheat ribbon*) with the p38α·DUSP10 MKBD complex (DUSP10 MKBD is shown as a *light blue ribbon*), illustrating the interaction of helix α2 with the p38α Φ_A pocket. Key residues from DUSP10 and DUSP16 are shown as *sticks* and labeled. *B*, same as *A* but illustrating the interaction of helix α3 with the p38α Φ_H pocket. Key residues from DUSP10 and DUSP16 are shown as *sticks* and labeled. *C*, same as *A* but illustrating the interaction of DUSP16 MKBD helix α4 with p38α. His-71 from DUSP16 is shown as *sticks* and labeled. *D*, raw isothermal titration calorimetry data (*upper panels*) and derived binding isotherm plotted *versus* the molar ratio of titrant fit using a one-site model (*lower panels*) for p38α with the DUSP16 MKBD H71A/S72A mutant.

S72A mutant is nearly identical to WT DUSP16 MKBD, showing that the protein is well folded in solution. As predicted, the measured K_D decreased about 2-fold (Fig. 5*D*, Table 1).

DISCUSSION

The activity of MAPKs is finely tuned in a cell type-specific and temporal manner by the concerted effort of multiple regulatory proteins. MAPKs are activated by a linear cascade of kinases, namely MAPKKKs and MAPKKs. In contrast, deactivation is highly diverse and achieved by a variety of phosphatases, including protein-Tyr-specific phosphatases (KIM-PTPs), dual specificity phosphatases (DUSPs, MKPs), and Ser/Thr phosphatases (*e.g.* protein phosphatase 2A (PP2A)). In particular, KIM-PTPs and DUSPs share a common MAPK interaction/anchoring site on MAPKs (13–15, 17, 19, 23, 39, 40), a site also used by MAPKKs (15, 41) and substrates (42–44). A comprehensive understanding of how the activity of MAPKs is finely controlled by their MAPK regulatory proteins can only be obtained by understanding how these proteins interact at a molecular level as it is the small structural and energetic differences between these proteins that ensure pathway fidelity.

Our work provides new insights into these subtle, yet critical differences. For example, a direct comparison of the K_D values between KIM peptides derived from KIM-PTPs (17, 19, 39) and MAPKs shows that the interaction between p38α and the DUSP16 MKBD, which contains a structured KIM, is ~5–10 times stronger. Furthermore, we show that the interaction of a MAPK with KIMs from proteins within a single family, namely the DUSP MKBDs, is also structurally distinct. Specifically, although the KIMs from KIM-PTPs or MAPKKs are flexible and linear, which allow them to interact with MAPKs in a continuous and extended manner, the binding possibilities of the KIMs from DUSP10 and DUSP16 are much more restricted as they are part of a well folded domain. Thus, the DUSP16 MKBD, like the DUSP10 MKBD, binds p38α via helices separated by loops that do not themselves continuously interact with p38α. The chain directionality is also different. Although most linear KIM peptides bind to the CD and hydrophobic pockets of MAPKs in an N-to-C-terminal direction, the DUSP

MKBDs bind differently, with the N-terminal helix α2 binding in the hydrophobic pocket and more C-terminal helix α3 binding at the CD site. This reversed directionality has also recently been identified in the linear KIM peptide from PEA-15 (44), and thus, it has become evident that the hydrophobic interaction site on MAPKs is bidirectional binding-competent. Interestingly, we have also recently shown that the family of KIM-containing PTPs bind very differently to p38α, showing that structural differences can account for the different activities of the regulatory enzymes (45).

Clearly, there are significant energetic and structural differences in the modes of interaction between MAPKs and their different families of regulatory proteins. Even more interesting, and what we show here, is that there are also key differences in these interactions between proteins from a single family. Specifically, although both DUSP10 and DUSP16 belong to the family of KIM-containing DUSPs that are selective for JNK and p38, there are clear differences in how they bind p38α. Although the DUSP10 MKBD primarily uses residues in helices α2 and α3 as well as part of the α2-α3 loop for its interaction with p38α, the DUSP16 MKBD uses not only residues in these helices but also residues in helix α4. Taken together, this additional binding surface leads to an enhanced interaction between these two proteins. This shows that although the α2 and α3 interaction is likely conserved between the family of DUSP MKBDs, the additional interactions of C-terminal (DUSP16) and potentially N-terminal residues in other DUSPs are likely important for different MAPK interaction strengths and, in turn, MAPK regulation and signal fidelity.

Acknowledgments—We thank Dr. D. Francis for help at different points in the project and Drs. L. Yang and M. Allaire (NSLS) for support at NSLS beamline X9. Use of NSLS at Brookhaven National Laboratory was supported by the United States Department of Energy, Office of Science, Office of Basic Energy Sciences under Contract Number DE-AC02-98CH10886. 800-MHz NMR data were recorded at Brandeis University (National Institutes of Health S10-RR017269). This research is based in part on data obtained at the Brown University Structural Biology Core Facility, which is supported by the Division of Biology and Medicine, Brown University.

REFERENCES

1. Chen, Z., Gibson, T. B., Robinson, F., Silvestro, L., Pearson, G., Xu, B., Wright, A., Vanderbilt, C., and Cobb, M. H. (2001) MAP kinases. *Chem. Rev.* **101,** 2449–2476
2. Kumar, S., Boehm, J., and Lee, J. C. (2003) p38 MAP kinases: key signalling molecules as therapeutic targets for inflammatory diseases. *Nat. Rev. Drug. Discov.* **2,** 717–726
3. Thalhamer, T., McGrath, M. A., and Harnett, M. M. (2008) MAPKs and their relevance to arthritis and inflammation. *Rheumatology* (*Oxford*) **47,** 409–414
4. Cohen, S., and Fleischmann, R. (2010) Kinase inhibitors: a new approach to rheumatoid arthritis treatment. *Curr. Opin. Rheumatol.* **22,** 330–335
5. Munoz, L., and Ammit, A. J. (2010) Targeting p38 MAPK pathway for the treatment of Alzheimer's disease. *Neuropharmacology* **58,** 561–568
6. Wang, G., Pan, J., and Chen, S. D. (2012) Kinases and kinase signaling pathways: potential therapeutic targets in Parkinson's disease. *Prog. Neurobiol.* **98,** 207–221
7. Lawan, A., Shi, H., Gatzke, F., and Bennett, A. M. (2013) Diversity and specificity of the mitogen-activated protein kinase phosphatase-1 functions. *Cell. Mol. Life Sci.* **70,** 223–237
8. Caunt, C. J., and Keyse, S. M. (2013) Dual-specificity MAP kinase phosphatases (MKPs): shaping the outcome of MAP kinase signalling. *FEBS J.* **280,** 489–504
9. Huang, C. Y., and Tan, T. H. (2012) DUSPs, to MAP kinases and beyond. *Cell Biosci.* **2,** 24
10. Goldsmith, E. J., Akella, R., Min, X., Zhou, T., and Humphreys, J. M. (2007) Substrate and docking interactions in serine/threonine protein kinases. *Chem. Rev.* **107,** 5065–5081
11. Goldsmith, E. J., Cobb, M. H., and Chang, C. I. (2004) Structure of MAPKs. *Methods Mol. Biol.* **250,** 127–144
12. Tárrega, C., Blanco-Aparicio, C., Muñoz, J. J., and Pulido, R. (2002) Two clusters of residues at the docking groove of mitogen-activated protein kinases differentially mediate their functional interaction with the tyrosine phosphatases PTP-SL and STEP. *J. Biol. Chem.* **277,** 2629–2636
13. Zhou, T., Sun, L., Humphreys, J., and Goldsmith, E. J. (2006) Docking interactions induce exposure of activation loop in the MAP kinase ERK2. *Structure* **14,** 1011–1019
14. Akella, R., Min, X., Wu, Q., Gardner, K. H., and Goldsmith, E. J. (2010) The third conformation of p38α MAP kinase observed in phosphorylated p38α and in solution. *Structure* **18,** 1571–1578
15. Chang, C. I., Xu, B. E., Akella, R., Cobb, M. H., and Goldsmith, E. J. (2002) Crystal structures of MAP kinase p38 complexed to the docking sites on its nuclear substrate MEF2A and activator MKK3b. *Mol. Cell* **9,** 1241–1249
16. Lee, T., Hoofnagle, A. N., Kabuyama, Y., Stroud, J., Min, X., Goldsmith, E. J., Chen, L., Resing, K. A., and Ahn, N. G. (2004) Docking motif interactions in MAP kinases revealed by hydrogen exchange mass spectrometry. *Mol. Cell* **14,** 43–55
17. Piserchio, A., Francis, D. M., Koveal, D., Dalby, K. N., Page, R., Peti, W., and Ghose, R. (2012) Docking Interactions of hematopoietic tyrosine phosphatase with MAP kinases ERK2 and p38α. *Biochemistry* **51,** 8047–8049
18. Piserchio, A., Warthaka, M., Devkota, A. K., Kaoud, T. S., Lee, S., Abramczyk, O., Ren, P., Dalby, K. N., and Ghose, R. (2011) Solution NMR insights into docking interactions involving inactive ERK2. *Biochemistry* **50,** 3660–3672
19. Francis, D. M., Różycki, B., Koveal, D., Hummer, G., Page, R., and Peti, W. (2011) Structural basis of p38α regulation by hematopoietic tyrosine phosphatase. *Nat. Chem. Biol.* **7,** 916–924
20. Barr, A. J., Ugochukwu, E., Lee, W. H., King, O. N., Filippakopoulos, P., Alfano, I., Savitsky, P., Burgess-Brown, N. A., Müller, S., and Knapp, S. (2009) Large-scale structural analysis of the classical human protein tyrosine phosphatome. *Cell* **136,** 352–363
21. Farooq, A., Chaturvedi, G., Mujtaba, S., Plotnikova, O., Zeng, L., Dhalluin, C., Ashton, R., and Zhou, M. M. (2001) Solution structure of ERK2 binding domain of MAPK phosphatase MKP-3: structural insights into MKP-3 activation by ERK2. *Mol. Cell* **7,** 387–399
22. Tao, X., and Tong, L. (2007) Crystal structure of the MAP kinase binding domain and the catalytic domain of human MKP5. *Protein Sci.* **16,** 880–886
23. Zhang, Y. Y., Wu, J. W., and Wang, Z. X. (2011) A distinct interaction mode revealed by the crystal structure of the kinase p38α with the MAPK binding domain of the phosphatase MKP5. *Sci. Signal.* **4,** ra88
24. Vogtherr, M., Saxena, K., Hoelder, S., Grimme, S., Betz, M., Schieborr, U., Pescatore, B., Robin, M., Delarbre, L., Langer, T., Wendt, K. U., and Schwalbe, H. (2006) NMR characterization of kinase p38 dynamics in free and ligand-bound forms. *Angew Chem. Int. Ed Engl.* **45,** 993–997
25. Vogtherr, M., Saxena, K., Grimme, S., Betz, M., Schieborr, U., Pescatore, B., Langer, T., and Schwalbe, H. (2005) NMR backbone assignment of the mitogen-activated protein (MAP) kinase p38. *J. Biomol. NMR* **32,** 175
26. Honndorf, V. S., Coudevylle, N., Laufer, S., Becker, S., and Griesinger, C. (2008) Dynamics in the p38α MAP kinase-SB203580 complex observed by liquid-state NMR spectroscopy. *Angew Chem. Int. Ed Engl.* **47,** 3548–3551
27. Honndorf, V. S., Coudevylle, N., Laufer, S., Becker, S., Griesinger, C., and Habeck, M. (2012) Inferential NMR/x-ray-based structure determination of a dibenzo[a,d]cycloheptenone inhibitor-p38α MAP kinase complex in solution. *Angew Chem. Int. Ed Engl.* **51,** 2359–2362
28. Delaglio, F., Grzesiek, S., Vuister, G. W., Zhu, G., Pfeifer, J., and Bax, A.

(1995) NMRPipe: a multidimensional spectral processing system based on UNIX pipes. *J. Biomol. NMR* **6,** 277–293
29. Goddard, T. D., and Kneller, D. G. (2006) *SPARKY 3*,University of California, San Francisco
30. de Vries, S. J., van Dijk, A. D., Krzeminski, M., van Dijk, M., Thureau, A., Hsu, V., Wassenaar, T., and Bonvin, A. M. (2007) HADDOCK versus HADDOCK: new features and performance of HADDOCK2.0 on the CAPRI targets. *Proteins* **69,** 726–733
31. Dominguez, C., Boelens, R., and Bonvin, A. M. (2003) HADDOCK: a protein-protein docking approach based on biochemical or biophysical information. *J. Am. Chem. Soc.* **125,** 1731–1737
32. Wang, Z., Harkins, P. C., Ulevitch, R. J., Han, J., Cobb, M. H., and Goldsmith, E. J. (1997) The structure of mitogen-activated protein kinase p38 at 2.1-Ä resolution. *Proc. Natl. Acad. Sci. U.S.A.* **94,** 2327–2332
33. Koradi, R., Billeter, M., and Wüthrich, K. (1996) MOLMOL: a program for display and analysis of macromolecular structures. *J. Mol. Graph.* **14,** 51–55, 29–32
34. Konarev, P. V., Volkov, V. V., Sokolova, A. V., Koch, M. H. J., and Svergun, D. I. (2003) PRIMUS: a Windows PC-based system for small-angle scattering data analysis. *J. Appl. Crystallogr.* **36,** 1277–1282
35. Svergun, D. (1992) Determination of the regularization parameter in indirect-transform methods using perceptual criteria. *J. Appl. Crystallogr.* **25,** 495–503
36. Svergun, D. I., Petoukhov, M. V., and Koch, M. H. (2001) Determination of domain structure of proteins from X-ray solution scattering. *Biophys. J.* **80,** 2946–2953
37. Volkov, V. V., and Svergun, D. I. (2003) Uniqueness of ab initio shape determination in small-angle scattering. *J. Appl. Crystallogr.* **36,** 860–864
38. Ortega, A., Amorós, D., and García de la Torre, J. (2011) Prediction of hydrodynamic and other solution properties of rigid proteins from atomic- and residue-level models. *Biophys. J.* **101,** 892–898
39. Francis, D. M., Różycki, B., Tortajada, A., Hummer, G., Peti, W., and Page, R. (2011) Resting and active states of the ERK2:HePTP complex. *J. Am. Chem. Soc.* **133,** 17138–17141
40. Liu, S., Sun, J. P., Zhou, B., and Zhang, Z. Y. (2006) Structural basis of docking interactions between ERK2 and MAP kinase phosphatase 3. *Proc. Natl. Acad. Sci. U.S.A.* **103,** 5326–5331
41. Garai, Á., Zeke, A., Gógl, G., Törő, I., Fördős, F., Blankenburg, H., Bárkai, T., Varga, J., Alexa, A., Emig, D., Albrecht, M., and Reményi, A. (2012) Specificity of linear motifs that bind to a common mitogen-activated protein kinase docking groove. *Sci. Signal.* **5,** ra74
42. White, A., Pargellis, C. A., Studts, J. M., Werneburg, B. G., and Farmer, B. T., 2nd. (2007) Molecular basis of MAPK-activated protein kinase 2: 38 assembly. *Proc. Natl. Acad. Sci. U.S.A.* **104,** 6353–6358
43. ter Haar, E., Prabhakar, P., Prabakhar, P., Liu, X., and Lepre, C. (2007) Crystal structure of the p38α-MAPKAP kinase 2 heterodimer. *J. Biol. Chem.* **282,** 9733–9739
44. Mace, P. D., Wallez, Y., Egger, M. F., Dobaczewska, M. K., Robinson, H., Pasquale, E. B., and Riedl, S. J. (2013) Structure of ERK2 bound to PEA-15 reveals a mechanism for rapid release of activated MAPK. *Nat. Commun.* **4,** 1681
45. Francis, D. M., Kumar, G. S., Koveal, D., Tortajada, A., Page, R., and Peti, W. (2013) The differential regulation of p38α by the neuronal KIM-PTPs, a detailed molecular study. *Structure*, DOI 10.1016/j.str.2013.07.003